Comparative Study of Manufacturing Techniques for Coronagraphic Binary Pupil Masks: Masks on Substrates and Free-Standing Masks

Keigo ENYA, Kanae HAZE, and Takayuki KOTANI

Department of Infrared Astrophysics, Institute of Space and Astronautical Science,
Japan Aerospace Exploration Agency 3-1-1 Yoshinodai, Chuo-ku, Sagamihara 229-8510
enya@ir.isas.jaxa.jp
and
Lyu ABE
Laboratoire Universitaire d'Astrophysique de Nice, UMR 6525, Parc Valrose, F-06108 Nice, France

Abstract

We present a comparative study of the manufacture of binary pupil masks for coronagraphic observations of exoplanets. A checkerboard mask design, a type of binary pupil mask design, was adopted, and identical patterns of the same size were used for all masks in order that we could compare the differences resulting from the different manufacturing methods. The masks on substrates had aluminum checkerboard patterns with thicknesses of $0.1/0.2/0.4/0.8/1.6 \, \mu$m, constructed on substrates of BK7 glass, silicon, and germanium using photolithography and chemical processes. Free-standing masks made of copper and nickel with thicknesses of $2/5/10/20 \, \mu$m were also realized using photolithography and chemical processes, which included careful release from the substrate used as an intermediate step in the manufacture. Coronagraphic experiments using a visible laser were carried out for all masks on BK7 glass substrate and the free-standing masks. The average contrasts were 8.4×10^{-8}, 1.2×10^{-7}, and 1.2×10^{-7} for the masks on BK7 substrates, the free-standing copper masks, and the free-standing nickel masks, respectively. No significant correlation was concluded between the contrast and the mask properties. The high-contrast masks have the potential to cover the needs of coronagraphs for both ground-based and space-borne telescopes over a wide wavelength range. Especially, their application to the infrared space telescope, SPICA, is appropriate.

Key words: instrumentation: high angular resolution — stars: planetary systems — telescopes

1. Introduction

The direct detection and spectroscopy of exoplanets is expected to play an essential role in the understanding of how planetary systems were born, how they evolve, and, ultimately, in finding biological signatures on these planets. For the direct observation of exoplanets, the enormous contrast in luminosity between the central star and the planet is a critical difficulty. For example, the contrast between the Sun and the Earth observed from outside is $\sim 10^{-10}$ at visible light wavelengths and $\sim 10^{-6}$ in the mid-infrared wavelength region, respectively (Traub & Jucks 2002). Therefore, the number of exoplanets detected directly is much smaller than the number of those detected by other methods (e.g., Mayor & Queloz 1995; Charbonneau et al. 2000), though the first direct observation was finally achieved (e.g., Marois et al. 2008; Kalas et al. 2008; Lagrange et al. 2010). Coronagraphs, which were first developed for solar observations (Lyot 1939), involve special optics to reduce the contrast. It is considered that advanced coronagraphs have a potential to make possible further extended direct observations of exoplanets.

Among the various current coronagraphic methods, coronagraphs using binary pupil masks have some advantages, and have been studied (Jacquinot & Roizen-Dossier 1964; Spergel 2001; Vanderbei et al. 2003a, 2003b, 2004; Kasdin et al. 2005a, 2005b; Belikov et al. 2007; Tanaka et al. 2006; Enya et al. 2007, 2008; Haze et al. 2009; Enya & Abe 2010; Carlotti et al. 2011; Haze et al. 2011; Enya et al. 2011a; Haze 2012). The function of a binary pupil mask coronagraph to produce a high-contrast point spread function (PSF) is to be less sensitive to wavelength (except the effect of scaling the size of the PSF), and also be much less sensitive to telescope pointing errors than other coronagraphs. Simplicity is another advantage of this optics. Because of these advantages, the use of a binary pupil mask coronagraph is being considered (e.g., Enya et al. 2011b) for the Space Infrared Telescope for Cosmology and Astrophysics (SPICA) mission (e.g., Nakagawa et al. 2009).

For the development of a binary pupil mask coronagraph, both free-standing masks and masks constructed on substrates are possible. In laboratory demonstration experiments, a high contrast of 6.7×10^{-8} was achieved with a high-precision mask constructed on a glass substrate by electron beam lithography (Enya et al. 2008). On the other hand, masks on substrates have undesirable properties. The substrates give rise to transmittance losses, and the applicable wavelength of the coronagraph is limited by the substrate material. Multiple reflections at the front and back surfaces of the mask are another disadvantage.
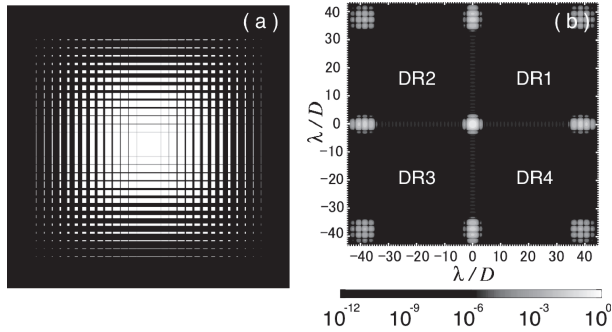
Considering this background, we carried out a comparative

Fig. 1. Mask design. Left: Design of the pupil mask. Optical transmittances of the black and white areas are 0 and 1, respectively. Right: Simulated PSF. Four dark regions (DRs), DR1–DR4, are produced around the core of the PSF.

Fig. 2. Geometry of the masks.

study of mask manufacturing processes. Aluminum (Al) mask patterns of various thicknesses were manufactured on substrates of BK7 glass, silicon (Si), and germanium (Ge). Free-standing masks made of copper (Cu) and nickel (Ni) of various thicknesses were also manufactured. The design of the mask pattern was common to all of the masks manufactured, so that we were able to carry out a systematic comparison of the coronagraphic performance while focusing on the differences in the manufacturing processes. In this work, we set the primary goal contrast to be 10^{-6} because of the need to observe exoplanets using space infrared telescopes. The design, manufacture, and the results of laboratory tests of the coronagraphic performance are presented in the following sections.

2. Mask Design

2.1. Checkerboard Pattern

Among the various binary pupil masks for coronagraphs, we chose the checkerboard mask for the following reasons: First, the topology of the checkerboard mask design essentially guarantees the possibility that it can be made as a free-standing mask. Second, the pattern consisting of many rectangular apertures formed of orthogonal straight lines is suitable for our manufacturing processes, rather than other masks consisting of apertures with smooth curves (e.g., Gaussian shaped masks). The design of the checkerboard pattern adopted in this work is shown in figure 1, in which four dark regions (DRs), DR1–DR4, are produced around the core of the PSF. The contrast, Inner Working Angle (*IWA*), and Outer Working Angle (*OWA*) in the design are 10^{10}, $5.4\,\lambda/D$, and $50\,\lambda/D$, respectively, in which λ is the wavelength and D is the length of the diagonal of the whole checkerboard pattern. It should be noted that the LOQO optimizer presented by Vanderbei (1999) was used for optimizing the design.

2.2. Variation

Table 1 summarizes the parameters of the various masks used in this work. For the material of the substrate, BK7 glass, Si, and Ge were adopted. Masks on BK7 glass substrates are convenient, since they can be tested with a visible light source at ambient temperature in air. Such tests for the masks on Si or Ge substrates are not possible because Si and Ge are opaque
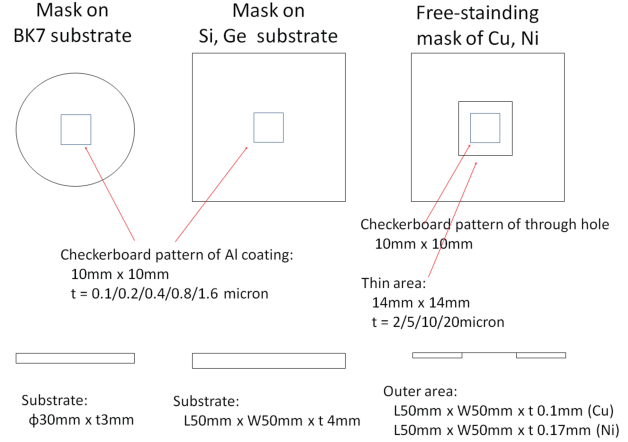
in the visible light wavelength region. On the other hand, masks on Si and Ge substrates can potentially be used in the mid-infrared wavelength region. The mask pattern was formed in Al of various thicknesses on all of these substrates. The thicknesses were $0.1/0.2/0.4/0.8/1.6\,\mu\mathrm{m}$. The free-standing masks were manufactured in various thicknesses of either Cu or Ni. We considered that high-precision manufacture with Cu is more common and established than Ni. On the other hand, Ni is physically tougher and more resistant to oxidation than Cu. The thicknesses of the free-standing masks were $2/5/10/20\,\mu\mathrm{m}$.

2.3. Geometry

The geometry of the masks is shown in figure 2. The geometry of the substrates was determined by the availability of those suitable for our manufacturing process. As a result, $\phi\,30\,\mathrm{mm}$ BK7 glass substrates, and $50\,\mathrm{mm}$-square Si and Ge substrates were selected. For all of the masks on substrates, the checkerboard pattern was located at the center of the substrate. The whole geometry of the free-standing masks was designed in order to actually realize "free-standing" and to make realistic holding possible. As a result, we adopted a $50\,\mathrm{mm}$-square design with a thicker holding area around the checkerboard pattern area. The goal thickness of the holder area in design is $\geq 100\,\mu\mathrm{m}$.

3. Manufacturing Processes

3.1. Photo-Mask for Micro-Structure Patterning

First, a photo-mask was manufactured on a special glass substrate, which used the master pattern of the micro-structure of all the coronagraphic masks manufactured in this work. Details of the manufacturing process for the photo-mask are shown below, and also in figure 3.

1. A special 4-inch (101.6 mm) square glass plate is used as the substrate.
2. The substrate is coated with $Cr + Cr_2 O_3$ ($0.1\,\mu\mathrm{m}$ thickness) by sputtering, a process in which a thin layer of metal is deposited by momentum exchange between energetic ions in a plasma and the atoms in a target material.

Table 1. Summary of mask specifications.

Type	No.	Mask	Thickness (μm)	Substrate	Note
on substrate	#SA001B	Al	0.1	BK7	AR*
	#SA002B	Al	0.2	BK7	AR*
	#SA004B	Al	0.4	BK7	AR*
	#SA008B	Al	0.8	BK7	AR*
	#SA016B	Al	1.6	BK7	AR*
	#SA001S	Al	0.1	Si	CL†
	#SA002S	Al	0.2	Si	CL†
	#SA004S	Al	0.4	Si	Failed‡
	#SA008S	Al	0.8	Si	Failed‡
	#SA016S	Al	1.6	Si	CL†
	#SA001G	Al	0.1	Ge	CL†
	#SA002G	Al	0.2	Ge	CL†
	#SA004G	Al	0.4	Ge	CL†
	#SA008G	Al	0.8	Ge	CL†
	#SA016G	Al	1.6	Ge	CL†
Free-standing	#FC020	Cu	2	—	
	#FC050	Cu	5	—	
	#FC100	Cu	10	—	
	#FC200	Cu	20	—	
	#FN020	Ni	2	—	
	#FN050	Ni	5	—	
	#FN100	Ni	10	—	
	#FN200	Ni	20	—	

* Anti-reflection coatings were applied to both sides.
† Cooling tests were applied.
‡ Manufacturing failed.

3. A 0.5 μm thick layer of photoresist is spin coated on the Cr$_2$O$_3$ layer. This procedure is used to make a uniform thin layer of photoresist on the substrate by rotating the substrate at high speed in order to spread the resist by centrifugal force.
4. Exposure: the micro-structure pattern is transferred to the photoresist using a laser (412 nm wavelength). Development: the photoresist (positive type) is removed.
5. The substrate is wet etched in an acid etch solution in a thin polyvinyl container.
6. The resist is stripped using a remover.

3.2. *Masks on Substrate*

Next, the masks on substrates were manufactured. ϕ 30 mm BK7 glass substrates, and 50 mm-square Si and Ge substrates were used. The detailed manufacturing process is shown below, and also in figure 4. Manufacture of the two masks, #SA004S and #SA008S, failed, and therefore these masks were not provided to the microscope check in the laboratory tests described in the nest section. The manufactured masks are shown in figure 6.

1. ϕ 30 mm BK7 glass, 50 mm-square Si, and 50 mm-square Ge are used as substrates.
2. Al with thicknesses of 0.1/0.2/0.4/0.8/1.6 μm is deposited on the substrates by EB vapor deposition, a process in which the aluminum is heated by an electron beam.

3. Photoresist with a thickness of 0.1 μm is spin coated on the Al.
4. Exposure: the pattern is transferred from the photo-mask to the photo-resist by UV light (365 nm wavelength) exposure. Development: The photoresist (positive type) is removed.
5. The substrate is wet etched in an acid etch solution in a thin polyvinyl container.
6. The photoresist is stripped by dipping in acetone.

3.3. *Free-Standing Masks*

Lastly, free-standing masks were manufactured. Details of the manufacturing process of free-standing masks of Cu are given below, and also in figure 5. The manufacturing process of free-standing masks of Ni are similar. The manufactured masks are shown in figure 6.

1. A special 4-inch (101.6 mm) square glass plate is used as the temporary substrate.
2. A sacrificial release layer with a thickness of 1 μm is spin-coated on the surface.
3. A seed layer of Cu (0.5 μm thickness) is deposited by EB vapor deposition on the release layer.
4. Resist (with a goal of 10 μm thickness) is spin-coated for plating on the Cu substrate.
5. Exposure: the patterns are transferred from the photo-mask to the photo-resist by exposure to UV light (365 nm
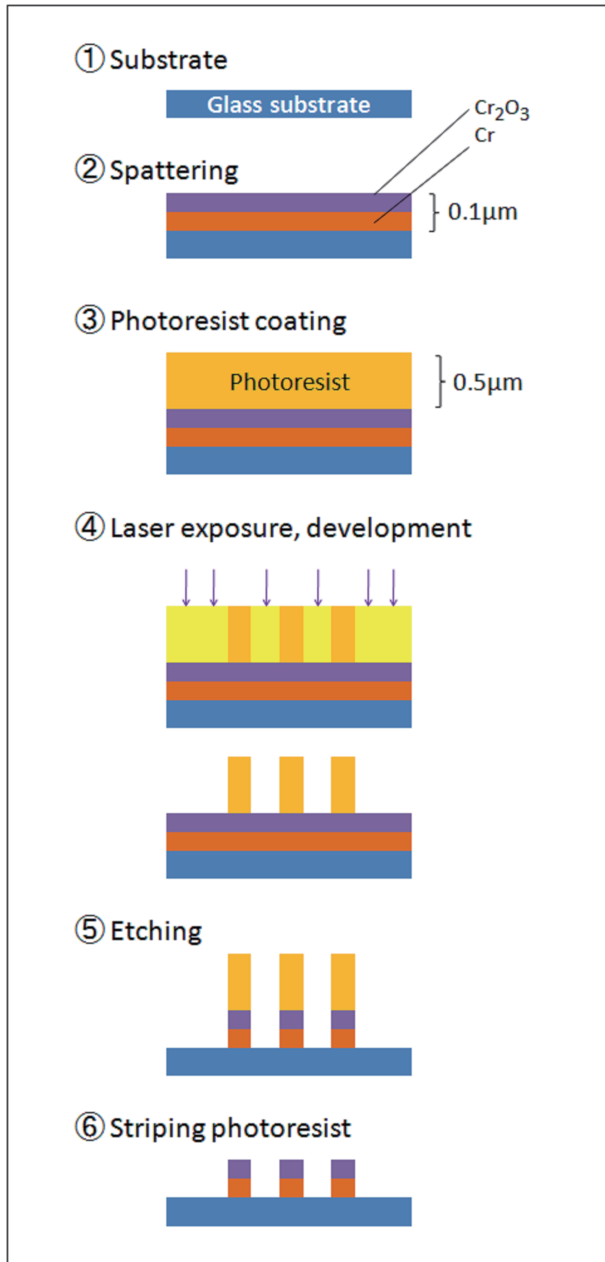
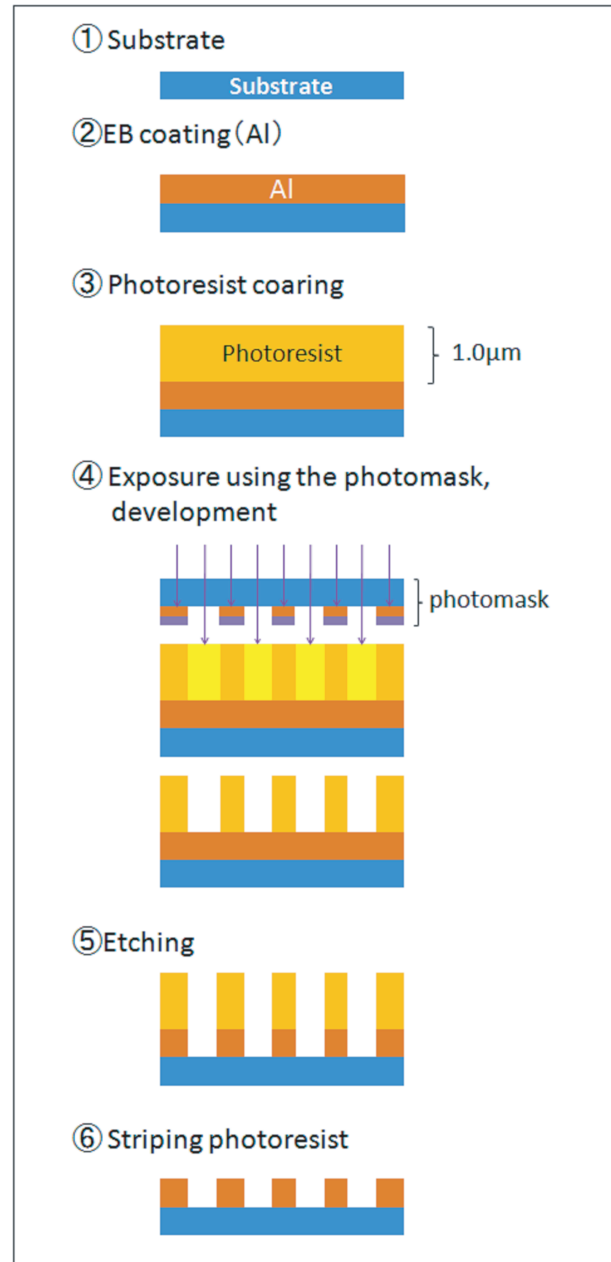**Fig. 3.** Manufacturing process of the photomask.

Fig. 4. Manufacturing process of masks on substrates.

wavelength). Development: the photo-resist is removed (only the illuminated part is dissolved, i.e., the resist is positive type).

6. Cu with goal thicknesses of 2/5/10/20 μm is grown by electrolytic plating, a process in which metal ions in solution are moved by an electric field to coat an electrode (i.e., the seed layer on the substrate).

7. The substrate is laminated with a dry film resist (100 μm thickness) to enable plating to be done for the support structure around the border of the central microstructure.

8. Exposure: the patterns are transferred from the photomask to the photoresist by UV light exposure

(365 nm wavelength). Development: the resist (negative type) is removed. Only the illuminated parts of the dry film resist remain.

9. A thick layer of Cu with a goal thickness of 100 μm is deposited by electrolytic plating.

10. The dry film resist is removed by dipping in acetone.

11. The photoresist is removed by dipping in acetone.

12. The Cu seed layer (0.5 μm thickness) is etched by wet etching the substrate in an acid etch solution in a thin polyvinyl container. Not only the seed layer but also 0.5 μm of Cu is removed in the process.

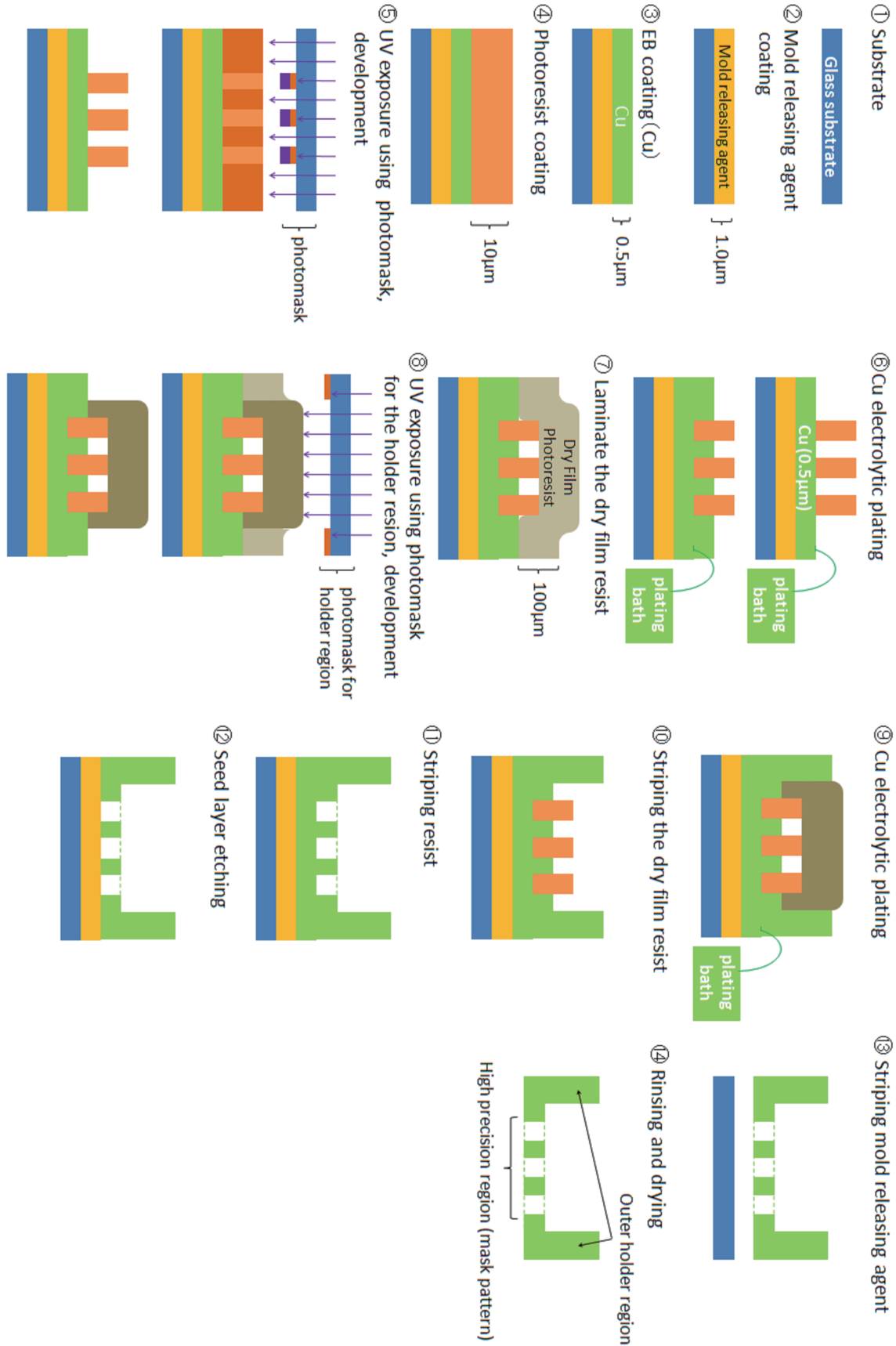13. The sacrificial release layer is removed by soaking in acetone.

Fig. 5. Manufacturing process of free-standing masks of Cu. Manufacturing process of free-standing masks of Ni are similar.

Fig. 6. Manufactured masks.

14. The substrate is rinsed in isopropyl alcohol, then dried naturally.

The achieved thickness of the holder area of the free-standing masks is $\sim 100\,\mu$m and $\sim 170\,\mu$m for Cu and Ni masks, respectively.

This work, a comparative study of mask manufacture, has been quested for several years (e.g., Enya 2008; Enya et al. 2011b). A free-standing mask of an early generation was used in Kotani et al. (2010), and improvements of the manufacture process have been continued. Recently, a free-stainding mask having the same specification with #FC020 was adopted in Haze (2012). It should be noted that there are confidential details in the manufacturing processes, which are not described in this section explicitly.

4. Laboratory Tests

4.1. Microscope Check

The manufactured masks were checked with a digital optical microscope, VHX-90 made by KEYENCE Co. Figures 7 and 8 show examples of the microscope images, cases for a mask on a BK7 glass substrate, #SA016B, and for a free-standing mask, #FC020, respectively. Since the role of the microscope check in this work is a qualifying round for the coronagraphic experiments, simply the topology of the mask was confirmed, rather than quantifying the imperfectness of the shape of many masks, i.e., we checked the following: (1) All of the holes in the design were reproduced in the manufactured masks. (2) There were no holes unexpected in the design, in the manufactured mask. (3) All of the holes in the design were separate from each other in the manufactured mask. All of the masks, except #SA004S
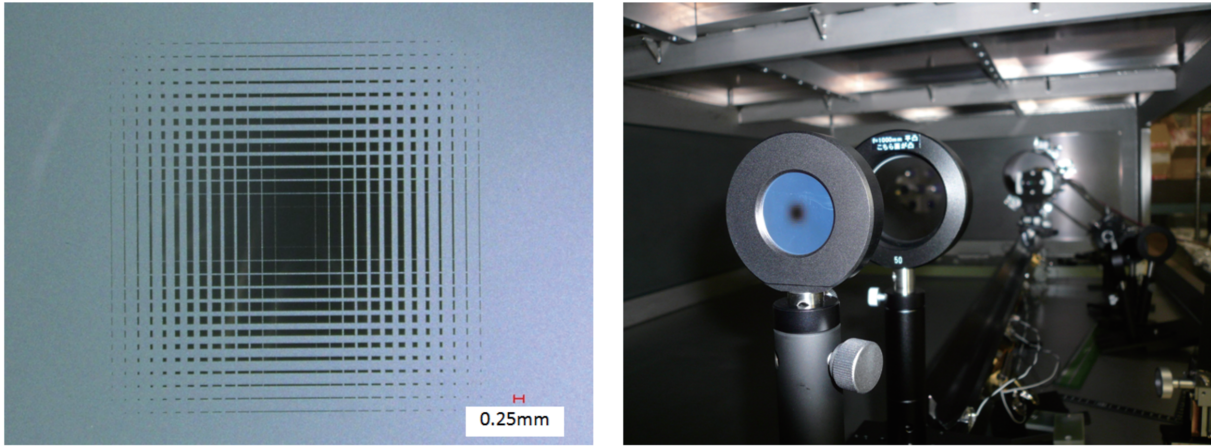
Fig. 7.   Left: Microscope image of a mask on a BK7 glass substrate, #SA016B. Right: Mask installed in the holder.
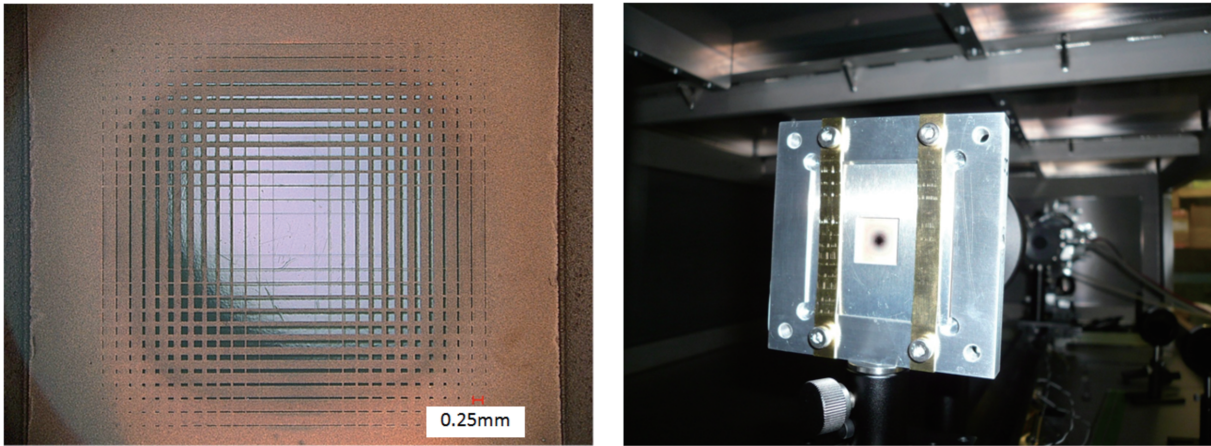

Fig. 8.   Left: Microscope image of a free-standing mask of Cu, #FC020. Right: Mask installed in the holder.

and #SA008S for which the manufacturing process had failed, passed the microscope check.

4.2.   Cooling Tests

The masks on Si and Ge substrate are designed to be operated at cryogenic temperature, and cooling them to low temperature could potentially delaminate them due to mechanical stresses induced by mismatch of the coefficient of thermal expansion between layers. We therefore carried out cooling tests for the masks on Si and Ge substrates. All masks were installed onto the cold worksurface of a cryostat in vacuum. The worksurface was connected to a liquid nitrogen tank with a thermal strap, and cooled by thermal conduction. The masks were cooled to $\sim 80\,\mathrm{K}$ in $10\,\mathrm{hr}$ (to $\sim 100\,\mathrm{K}$ in $2\,\mathrm{hr}$), and then warmed up to ambient temperature in $20\,\mathrm{hr}$. Lastly microscopic check was applied, and it confirmed that no delamination was found for all cooled masks.

4.3.   Coronagraphic Experiments

Coronagraphic experiments were carried out on all of the masks with BK7 glass substrates and the free-standing masks. The configuration of the experiment is shown in figure 9,
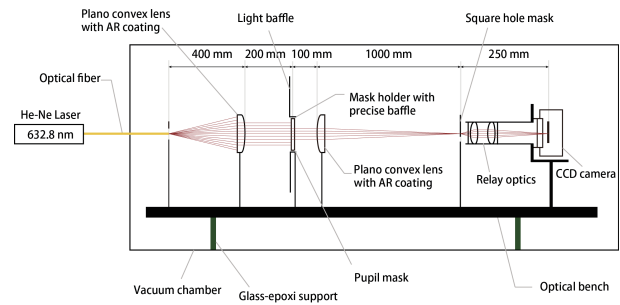

Fig. 9.   Configuration of the coronagraphic experiment.

which, except for the masks and their holders, is basically the same as the setup shown in subsection 2.4 of Haze (2012). The optics were placed in a vacuum chamber, but vacuum pumping was not applied for the experiment presented in this paper. Figures 7 and 8 show examples of a mask installed in the holder, cases for a mask on a BK7 glass substrate, #SA016B, for a free-standing mask, #FC020, respectively. All of the coronagraphic images were taken using light passing through
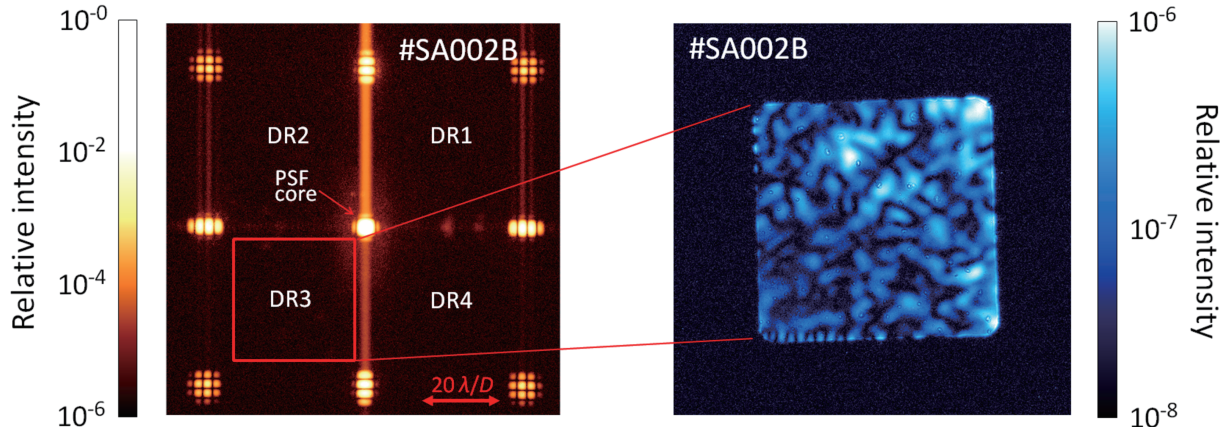
Fig. 10. Coronagraphic image taken with a mask on a BK7 glass substrate, #SA002B. Left: Image includes the core of the PSF. Right: High sensitivity image of the DR taken with a square hole mask.
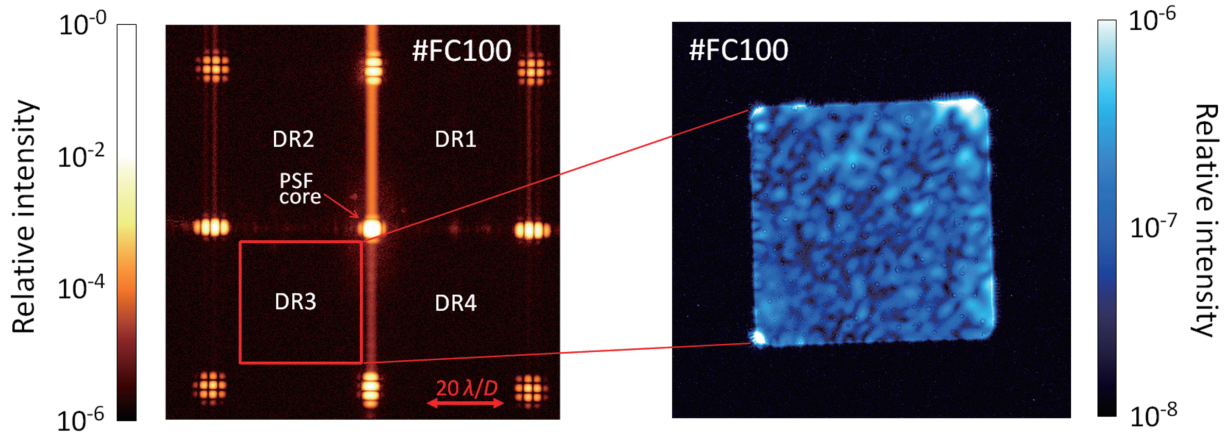

Fig. 11. Coronagraphic image taken with a free-standing mask of Cu, #FC100. Left: Image includes the core of the PSF. Right: High sensitivity image of the DR taken with a square hole mask.

the mask (i.e., reflected light was not used). A 632.8 nm wavelength He-Ne laser was used as the light source, and this was introduced into the chamber through a single mode fiber. All of the focusing and collimation were executed with a plano-convex lens with anti-reflection coatings on both surfaces. A CCD camera set in the chamber was used to take coronagraphic images. Relay optics ($\times 3.4$ magnification) were set after the focal plane mask to obtain proper image sizes. To realize high dynamic-range measurements, the cores and the DRs of the coronagraphic PSFs were taken separately. For each mask, we evaluated only the DR3 of the four DRs shown in figure 1, because of a consideration for the efficiency of the experiment in this work. The core images were taken with exposure times of 0.03/0.3/3 s using two ND filters with a total optical density of 4. The DR of the coronagraphic image was observed with a 300 s exposure using a square-hole focal-plane mask, without the ND filters. For all images, dark frames were taken with the same configuration, with the same exposure time, but with the light source turned off. The dark frame was subtracted from the corresponding coronagraphic image, and then the raw image of the coronagraphic PSF was obtained.

The observed coronagraphic PSFs for a mask on a BK7 glass substrate, #SA002B, are shown in figure 10, in which the left and right panels are the image including the core, and the high sensitivity image of the DR, respectively. The observed coronagraphic PSFs taken with a free-standing mask of Cu, #FC100, are also shown in figure 11. In both cases, the observed core images are quite similar to the ones expected from the design presented in figure 1. On the other hand, the observed dark images are filled with irregular speckle patterns. This feature, core images expected from the design and the DR filled with speckle, was commonly found in all of the coronagraphic PSFs obtained in this work. Diagonal profiles of the coronagraphic images obtained from the masks with BK7 glass substrates and the free-standing Cu and Ni masks are presented in figure 12.

For all of the masks tested in the coronagraphic experiments, the contrast was derived as the intensity ratio between the peak of the core and the linear average of the DR. The contrasts obtained are presented in table 2.

5. Discussion and Summary

The contrasts obtained are distributed from 5.3×10^{-8} to 2.1×10^{-7}. It should be noted that all of the contrasts exceed
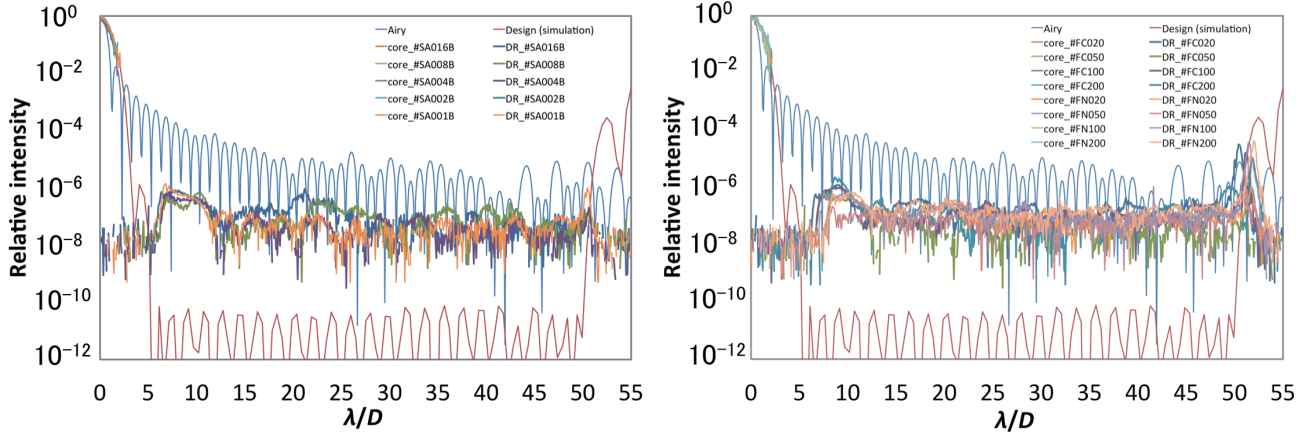
Fig. 12. Left: Diagonal profiles of coronagraphic images obtained with masks on BK7 substrate. Right: Diagonal profiles of coronagraphic images obtained with free-standing masks.

Table 2. Contrast obtained by experiment.

No.	Contrast	No.	Contrast	No.	Contrast
#SA001B	6.6×10^{-8}	#FC020	2.1×10^{-7}	#FN020	1.1×10^{-7}
#SA002B	1.1×10^{-7}	#FC050	5.3×10^{-8}	#FN050	8.5×10^{-8}
#SA004B	5.9×10^{-8}	#FC100	1.1×10^{-7}	#FN100	1.2×10^{-7}
#SA008B	7.3×10^{-8}	#FC200	9.3×10^{-8}	#FN200	1.8×10^{-7}
#SA016B	1.1×10^{-7}				
Average	8.4×10^{-8}		1.2×10^{-2}		1.2×10^{-7}

the goal set at the beginning of this work, 10^{-6}. The average contrasts were 8.4×10^{-8}, 1.2×10^{-7}, and 1.2×10^{-7} for the masks on the BK7 glass substrates, and the free-standing masks of Cu and Ni, respectively. The average contrast for the masks on the BK7 glass substrates is higher than those of the free-standing masks. However, because of the dispersion of the data, the statistical significance of this is not valid. Also, a significant correlation is not concluded between the contrast and the mask thickness for each of the three types of mask.

Because the contrast in the design is 10^{-10}, it is obvious that there is a practical limiting factor that gives rise to speckle patterns observed in the DRs. However, identification of this limiting factor was not easy. Using a mask having the same specification with #FC020, a detailed study about the limiting factor was performed, as shown in Haze (2012). For example, mask-rotation methods were tested. In these tests, it is expected that the speckle patterns are rotated with the mask if the speckle patterns were produced simply by an error of the mask shape. However, less correlation was confirmed between the speckle pattern before and after the mask rotation. Finally, suggested candidates of the limiting factor are imperfectness of the incident beam (e.g., wavefront error, inhomogeneity of amplitude, and so on) and error in the repeatability of the mask position before and after rotation. The influence of the instability of the experimental system is also suggested. For more details, please see Haze (2012).

The wavefront error can be corrected by using deformable mirrors. Trauger and Traub (2007) pioneered ultra high contrast using wavefront control with High Contrast Imaging Testbed. Using one of early generations of our free-standing mask, Kotani et al. (2010) demonstrated an improvement of the contrast by a factor of ~ 100 at a part of the dark region close to *IWA* in the air with a visible laser. For use in the infrared wavelength region, the development of a cryogenic deformable mirror is ongoing. Actuation of a proto-type of Micro Electro Mechanical Systems (MEMS) deformable mirror with 32 actuators was demonstrated at ~ 95 K (Enya et al. 2009). Toughness tests, vibration tests, and rapid pumping tests were also carried out for the proto-type (Enya et al. 2011a).

Coronagraphic experiments for the masks on Ge and Si substrates were not carried out in this work, since visible light was used as the light source and the experiments were carried out at ambient temperature in air. Important future work is to demonstrate the coronagraphic performance directly in the mid-infrared wavelength region at cryogenic temperatures in a vacuum. The following results, indirectly, suggest the applicability of the masks on Ge and Si substrates: (1) High contrast was achieved using the masks on BK7 glass substrates in this work. (2) The masks on Ge and Si substrates and the masks on BK7 glass substrates were manufactured using the same process. (3) The masks on Ge and Si substrates survived the cooling tests. It is also important to evaluate the coronagraph using free-standing masks in infrared at cryogenic temperature. Finally, the performances of the all the masks for an infrared coronagraph should be compared.

Only one mask design, a checkerboard type without pupil obscuration, was used in this work to compare the various manufacturing processes. On the other hand, recent progress in mask design allows the binary pupil mask coronagraph to be applied to normal telescopes with pupil obscuration, which is not specially designed for a coronagraph. Carlotti, Vanderbei, and Kasdin (2011) presented a 2-dimensionally optimized pupil design that provides the ultimate efficiency possible in terms of throughput for a pupil coronagraph mask. An integral 1-dimensional coronagraph pupil mask also gives a higher throughput than conventional ones, and a generalized design of the dark region at the focal plane was introduced to realize a more efficient distribution of the *IWA*, *OWA*, and contrast at the focal plane (Enya & Abe 2010; Enya et al. 2011a). As a result, these high-contrast masks have potential to cover the needs of coronagraphs for ground-based telescopes (e.g., current 8–10 m class telescopes like SUBARU, and larger future ones such as TMT, EELT), and space telescopes (e.g., JWST, SPICA) over a wide wavelength region. Indeed, the use of a binary pupil mask coronagraph is planned for the SPICA Coronagraph Instrument (SCI), for which the results of this work are quite encouraging. Because of less wavelength dependence of binary pupil mask coronagraphs, it would be worthy to evaluate the benefit of applying binary pupil masks to instruments used in SPICA for longer wavelengths; Mid-infrared Camera and Spectrometer (MCS: Kataza et al. 2010) and/or SPICA FAR-infrared Instrument (SAFARI: e.g., Goicoechea et al. 2011).

In the work presented in this paper, we carried out a comparative study of the manufacturing processes of binary pupil masks for coronagraphs. Both masks on substrates and free-standing masks were manufactured with various materials and thicknesses. Coronagraphic experiments in the visible light region confirmed the high contrast, in which the obtained average contrasts were 8.4×10^{-8}, 1.2×10^{-7}, and 1.2×10^{-7} for the masks on BK7 substrates, the free-standing copper masks, and the free-standing nickel masks, respectively. A significant correlation was not concluded between the contrast and the mask properties. We consider that such masks have potential to cover the needs of coronagraphs for various telescopes.

References

Belikov, R., et al. 2007, Proc. SPIE, 6693, 66930Y

Carlotti, A., Vanderbei, R., & Kasdin, N. J., 2011, arXiv:1108.4050

Charbonneau, D., Brown, T. M., Latham, D. W., & Mayor, M. 2000, ApJ, 529, L45

Enya, K. 2008, Abstract, 37th COSPAR Scientific Assembly, 812

Enya, K., et al. 2011b, Adv. Space Res., 48, 323

Enya, K., & Abe, L. 2010, PASJ, 62, 1407

Enya, K., Abe, L., Takeuchi, S., Kotani, T., & Yamamuro, T. 2011a, Proc. SPIE, 8146, 81460Q

Enya, K., Abe, L., Tanaka, S., Nakagawa, T., Haze, K., Sato, T., & Wakayama, T. 2008, A&A, 480, 899

Enya, K., Kataza, H., & Bierden, P. 2009, PASP, 121, 260

Enya, K., Tanaka, S., Abe, L., & Nakagawa, T. 2007, A&A, 461, 783

Goicoechea, J. R., Roelfsema, P. R., Jellema, W., & Swinyard, B. M. Poster presented at IAU Symp. 280, The Molecular Universe, Toledo, Spain, May 2011, #179

Haze, K. 2012, PhD. Thesis, The Graduate University for Advanced Studies (arXiv1112.6301H)

Haze, K., Enya, K., Abe, L., Kotani, T., Nakagawa, T., Sato, T., & Yamamuro, T. 2011, PASJ, 63, 873

Haze, K., Enya, K., Abe, L., Tanaka, S., Nakagawa, T., Sato, T., Wakayama, T., & Yamamuro, T. 2009, Adv. Space Res., 43, 181

Jacquinot, P., & Roizen-Dossier, B. 1964, Prog. Opt., 3, 29

Kalas, P., et al. 2008, Science, 322, 1345

Kataza, H., Wada, T., Ikeda, Y., Fujishiro, N., Kobayashi, N., & Sakon, I. 2010, Proc. SPIE, 7731, 77314A

Kasdin, N. J., Vanderbei, R. J., Littman, M. G., & Spergel, D. N. 2005a, Appl. Opt., 44, 1117

Kasdin, N. J., Belikov, R., Beall, J., Vanderbei, R. J. Littman, M. G., Carr, M., & Give'on, A. 2005b, Proc. SPIE, 5905, 59050G

Kotani, T., et al. 2010, in ASP Conf. Proc., 430, Pathways Towards Habitable Planets, ed. V. Coudé du Foresto (San Francisco: ASP), 477

Lagrange, A.-M., et al. 2010, Science, 329, 57

Lyot, M. B. 1939, MNRAS, 99, 580

Marois, C., Macintosh, B., Barman, T., Zuckerman, B., Song, I., Patience, J., Lafrenière, D., & Doyon, R. 2008, Science, 322, 1348

Mayor, M., & Queloz, D. 1995, Nature, 378, 355

Nakagawa, T., & Spica Team 2009, in Proc. SPICA joint European/Japanese Workshop, ed. A. M. Heras et al. (Les Ulis: EDP Sciences), 01001

Spergel, D. N., 2001, arXiv:astro-ph/0101142

Tanaka, S., Enya, K., Abe, L., Nakagawa, T., & Kataza, H. 2006, PASJ, 58, 627

Traub, W. A., & Jucks, K. W. 2002, in Atmospheres in the Solar System: Comparative Aeronomy, ed. M. Mendillo et al. (Washington D.C.: AGU), 369

Trauger, J. T., & Traub, W. A. 2007, Nature, 446, 771

Vanderbei, R. J. 1999, Optimization methods and software, 11, 451

Vanderbei, R. J., Kasdin, N. J., & Spergel, D. N. 2004, ApJ, 615, 555

Vanderbei, R. J., Kasdin, N. J., & Spergel, D. N. 2003, ApJ, 590, 593

Vanderbei, R. J., Spergel, D. N., & Kasdin, N. J. 2003, ApJ, 599, 686